

## 2D hetero-nanosheets to enable ultralow thermal conductivity by all scale phonon scattering for highly thermoelectric performance

Shuankui Li<sup>a</sup>, Chao Xin<sup>a</sup>, Xuerui Liu<sup>a</sup>, Yancong Feng<sup>a</sup>, Yidong Liu<sup>a</sup>, Jiaxin Zheng<sup>a</sup>, Fusheng Liu<sup>b</sup>, Qingzhen Huang<sup>c</sup>, Yiming Qiu<sup>c</sup>, Jiaqing He<sup>d</sup>, Jun Luo<sup>a</sup>, Feng Pan<sup>a,\*</sup>

<sup>a</sup> School of Advanced Materials, Peking University Shenzhen Graduate School, Shenzhen 518055, China

<sup>b</sup> College of Materials Science and Engineering, Shenzhen University and Shenzhen Key Laboratory of Special Functional Materials, Shenzhen 518060, China

<sup>c</sup> NIST Center for Neutron Research, National Institute of Standards and Technology, Gaithersburg, MD 20899-6102, USA

<sup>d</sup> Department of Physics, South University of Science and Technology of China, Shenzhen 518055, China

### ARTICLE INFO

#### Keywords:

Thermoelectric materials

Bi<sub>2</sub>Te<sub>3</sub>

Nanostructure

Heterogeneous

Phonon scattering

### ABSTRACT

It remains a great challenge to design thermoelectric materials with high figure of merit ZT because of the strongly correlated material parameters such as the electrical conductivity, thermal conductivity, and Seebeck coefficient, which restricts the maximum ZT values to ~1 in bulk thermoelectric materials. Here, we demonstrate a strategy based on nanostructuring and alloying to synthesize the two-dimensional (2D) Bi<sub>2</sub>Te<sub>2.7</sub>So<sub>0.3</sub>/Bi<sub>2</sub>Te<sub>3</sub> hetero-nanosheet with atomically thin heterojunction interfaces to optimize the electron and phonon transport behavior. A full-spectrum phonons scattering has been achieved to enable ultralow thermal conductivity by the atomic-scale alloy and defect to target high frequency phonons, heterojunction interface to target mid-frequency phonons, and nanoscale grains boundary to target low-frequency phonons. With this technique, the lattice thermal conductivity ( $\kappa_{\text{latt}}$ ) is dramatically reduced to 0.2–0.3 W m<sup>-1</sup> K<sup>-1</sup> near the lower limit of the randomly oriented  $\kappa_{\text{latt}}$  (0.18 W m<sup>-1</sup> K<sup>-1</sup>), but the electrical transport properties is well maintained. Taking advantage of the maximumly reduced thermal conductivity as well as the maintained power factors, the maximum ZT reaches 1.17 and 0.9 at 450 K and around room temperature, respectively, approximately three times higher than their counterparts without atomically thin heterostructure.

### 1. Introduction

Thermoelectric (TE) materials for generating electricity directly from waste heat have attracted increasing attention due to its potential to provide a clean and efficient way to solve the energy crisis and reduce the greenhouse gas emissions [1–3]. It is well known that the energy conversion efficiency of TE materials is defined by the dimensionless figure of merit  $ZT = S^2\sigma T/\kappa$ , which depends on the Seebeck coefficient (S), electrical conductivity ( $\sigma$ ), electronic and lattice thermal conductivity ( $\kappa$ ), and absolute temperature (T) [4,5]. However, these transport properties ( $\sigma$ , S, and  $\kappa$ ) are not only highly interdependent but also conflicted with each other. For example, TE materials always have both high electrical and thermal conductivity together, because these transport properties are all determined by the basic electronic structure (band gap, band shape, and band degeneracy near the Fermi level) and scattering of charge carriers (electrons or holes) of the TE materials [6–14]. Hierarchical and heterogeneous architecture with molecular/nano/micro-structure engineering are the most promising approaches to improve the ZT value, since the molecules with heavy

atoms, heterogeneous interfaces, and nano/micrograins can scatter phonons with different frequencies, leading to a dramatic reduction of the thermal conductivity. Meanwhile, the quantum effects and low energy carrier filtering at the designed boundaries can enhance power factor significantly. However, it is still a great challenge for designing TE materials to satisfy the criteria with a combination of both high power factor and low total thermal conductivity synchronously [15,16].

As one of the best TE materials working around room temperature, Bi<sub>2</sub>Te<sub>3</sub> (BT) and its based alloys have been widely studied in recent years because of their high electrical conductivity determined by the narrow band gap as well as relatively low thermal conductivity [17–19]. Furthermore, introducing proper doping, such as Sb (at Bi sites) and Se (at Te sites), to the Bi<sub>2</sub>Te<sub>3</sub> materials could greatly improve the TE performances [20,21]. As for the case of Bi<sub>2</sub>Te<sub>3-x</sub>Se<sub>x</sub>, the solubility of Se in Bi<sub>2</sub>Te<sub>3</sub> can reduce the thermal conductivity and enhance the power factor by modifying the crystalline structure and electronic density of states. With the advent of nanotechnology, Bi<sub>2</sub>Te<sub>3</sub>-based nanomaterials with complex heterogeneous nanostructure are considered to be promising TE materials, as the incorporation of multi phases

\* Corresponding author.

E-mail addresses: [luojun@pkusz.edu.cn](mailto:luojun@pkusz.edu.cn) (J. Luo), [panfeng@pkusz.edu.cn](mailto:panfeng@pkusz.edu.cn) (F. Pan).

<http://dx.doi.org/10.1016/j.nanoen.2016.09.018>

Received 12 July 2016; Received in revised form 7 September 2016; Accepted 11 September 2016

Available online 12 September 2016

2211-2855/ © 2016 Elsevier Ltd. All rights reserved.

provides an opportunity to produce a unique electron (carrier) transport behavior, which can decouple electron transport from the phonon scattering at the interfaces [22,23]. Therefore, with properly designed heterojunction interfaces, the TE materials with high performance, which are expected to possess low thermal conductivity without degrading the power factor in the conflicting pairs, could be obtained [24]. In this work, we design and fabricate the novel hierarchical  $\text{Bi}_2\text{Te}_3$ -based TE materials with a BTS/BT hybrid structure by the following approaches: controlling the molecular composition with BTS/BT ratio, formation of single/few-layer BT seed-crystals by chemical exfoliation, BTS layer-epitaxial growth along BT layer-seeds to form two-dimensional (2D) hetero-nanosheets, and combination of BTS/BT 2D sheets to generate optimized boundaries with the simple and low-cost synthetic processes. It is found that such unique structure can scatter all scale phonons in different frequencies effectively to achieve ultralow thermal conductivity.

## 2. Experimental section

### 2.1. Materials

Bulk  $\text{Bi}_2\text{Te}_3$  (99.999%) was purchased from alfa aesar;  $\text{TeO}_2$  powder (99.999%),  $\text{SeO}_2$  powder (99.999%),  $\text{Bi}(\text{NO}_3)_3 \cdot 5\text{H}_2\text{O}$ ,  $\text{Li}_2\text{CO}_3$ , Sodium Hydroxide, Vitamin C, ethylene glycol, dimethylformamide (DMF), acetone, ethanol and HCl were purchased from the Shanghai Reagent Company. All the chemicals were used as obtained without further purification.

### 2.2. Synthesis of $\text{Bi}_2\text{Te}_3$ single layers

In this work, we obtained the  $\text{Bi}_2\text{Te}_3$  single layers via a solvent exfoliation technique of  $\text{Bi}_2\text{Te}_3$  ingot samples as described in previous report [29]. For the synthesis of  $\text{Bi}_2\text{Te}_3$  single layers, 0.5 g bulk  $\text{Bi}_2\text{Te}_3$  and 0.7 g  $\text{Li}_2\text{CO}_3$  were added into a mixture solution with 40 ml benzyl alcohol and 40 ml DMF under magnetic stirring. The resulting solution was transferred into a Teflon-lined stainless autoclave (100 ml capacity), followed by solvothermal treatment at 220 °C for 72 h. The product was collected by filtration, successively washed several times with deionized water and absolute ethanol. Then, the as obtained Li-intercalated  $\text{Bi}_2\text{Te}_3$  microplates dispersed in 200 ml beaker with a mixture solution of 100 ml distilled water and 100 ml DMF. The beaker was then sealed and sonicated at a low power sonic bath for 6 h. The resultant dispersions were centrifuged at 500 rpm for 5 min to remove the unexfoliated  $\text{Bi}_2\text{Te}_3$  microplates and centrifuged at 12000 rpm for 5 min. The as-obtained products were rinsed with 3% HCl for two times to eliminate the excess  $\text{Li}_2\text{CO}_3$  and then washed by the distilled water until neutrality. After the treatment, the products were collected by filtration, successively washed several times with deionized water and absolute ethanol, and dried at 60 °C for 24 h.

### 2.3. Synthesis of $\text{Bi}_2\text{Te}_{2.7}\text{Se}_{0.3}/\text{Bi}_2\text{Te}_3$ 2D hetero-nanosheet

For the synthesis of the 2D hetero-nanosheet, 60 ml of ethylene glycol is added to a three-neck flask equipped with a standard schlenk line, followed by adding of 2.4 g of NaOH, 1.74 g  $\text{TeO}_2$  and 0.133 g  $\text{SeO}_2$  powder under magnetic stirring until all of them dissolved. For the synthesis of the Bi precursor solution, an amount of as-prepared  $\text{Bi}_2\text{Te}_3$  single layers dispersed in another 20 ml ethylene glycol. After sonicated at a low power sonic bath for 1h, the 3.88 g of  $\text{Bi}(\text{NO}_3)_3 \cdot 5\text{H}_2\text{O}$  and 0.528 g Vitamin C were added to the as-prepared mixture solution. For the synthesis of 2D hetero-nanosheet, the three-neck flask is heated to 160 °C under nitrogen protection and then as-prepared Bi precursor solution is injected into the above solution at 160 °C. After reaction for another 2 h, the products were collected by filtration, successively washed several times with deionized water and absolute ethanol, and dried at 60 °C for 24 h. In this work, the sample  $\text{Bi}_2\text{Te}_{2.7}\text{Se}_{0.3}$  and

$\text{Bi}_2\text{Te}_3$  were denoted as BTS and BT respectively. The as-synthesized  $\text{Bi}_2\text{Te}_{2.7}\text{Se}_{0.3}/\text{Bi}_2\text{Te}_3$  2D hetero-nanosheet with different as-exfoliated  $\text{Bi}_2\text{Te}_3$  contents were denoted as BTS/BTx, in which x is the contents of as-exfoliated  $\text{Bi}_2\text{Te}_3$  (x mg). The sample prepared by mixing the as-prepared BTS nanosheet with 90 mg few-layers BT using ultrasonic dispersion treatment noted as BTS/BT90mixture.

### 2.4. Characterisation

X-ray diffraction (XRD) was performed on a Bruker D8 Advance powder X-ray diffractometer; field-emission scanning electron microscopy (SEM) on a Zeiss SUPRA-55; transmission electron microscopy (TEM) on a JEOL-2010 instrument. X-ray photoelectron spectra (XPS) were acquired on Thermo Fisher ESCALAB 250X surface analysis system equipped with a monochromatized Al anode X-ray source (X-ray photoelectron spectroscopy, XPS,  $h\nu=1486.6$  eV). Raman spectra were detected by a HoribaHR320 Raman spectrometer with a 532 nm Ar laser. Atomic force microscopy (AFM) study was performed by means of A Bruker MultiMode 8 AFM.

### 2.5. Thermoelectric measurements

The dry powders pressed into pellets by spark plasma sintering (SPS) at 573 K for 5 min under a vacuum with a uniaxial pressure of 40 MPa. The electrical conductivity and Seebeck coefficient were simultaneously measured by the standard four-probe methods under a helium atmosphere using ausing ULVAC ZEM-3 within the temperature range 300–480 K. The thermal conductivity ( $\kappa$ ) was calculated through  $\kappa=DC_p\rho$ , where D,  $C_p$ , and  $\rho$  are the thermal diffusivity coefficient, specific heat capacity, and density, respectively. The thermal diffusivity coefficient was measured by a laser flash apparatus using Netzsch LFA 457 from 300 to 480 K, and the specific heat ( $C_p$ ) was tested by a differential scanning calorimeter (Mettler DSC1), and the density ( $\rho$ ) was calculated by using the mass and dimensions of the pellet. The porosity of the samples was determined using the equation  $\phi=(\rho_0-\rho)/\rho_0$ , where  $\rho_0$  is the absolute density of the materials with the same composition.

## 3. Results and discussion

BT is a type of anisotropic layered material with R3-m space group, in which each quintuple layer composed of five covalently bonded atomic planes [ $\text{Te}_1\text{-Bi-Te}_2\text{-Bi-Te}_1$ ] is adhered together by weak van der Waals interactions along the c-axis (Fig. 1a) [25]. Owing to the intrinsically anisotropic bonding nature caused by the weak van der Waals interaction between the adjacent  $\text{Te}_1$  atomic planes, BT could be easily disassembled along the c-axis to achieve the single/few-layered samples by the chemical exfoliation method [26]. Compared with the bulk material, the metallic surface states of single/few-layered BT generate the unique 2D electron gas that covers the whole surface, ensuring high electron mobility and Fermi velocity [27,28]. Herein we have synthesized the few-layers (less than 5 layers) BT via a scalable chemical intercalation/exfoliation strategy as described in previous report [29]. Upon chemical exfoliation, the layer dimensions are reduced to about 500 nm in length and 2 nm in thickness as observed by TEM (Fig. 2) and AFM (Fig. S1). The Raman spectroscopy confirms the presence of exfoliation-induced defect centers (Fig. S2). At low frequency region (60–150  $\text{cm}^{-1}$ ), the peaks at 125 and 168  $\text{cm}^{-1}$  assigned as  $E_g^2$  and  $A_1g^2$  modes present in all samples, and no discernible shift in the Raman peak positions is observed. Interestingly, for the as-exfoliated few-layers BT, the intensity of the peak at 760  $\text{cm}^{-1}$  increases sharply, which might be attributed to the combination and overtone modes due to defect-induced symmetry breaking [28]. This phenomenon means that the as-exfoliated few-layers BT has numerous exfoliation-induced defect centers in both plane and edge, which plays a key role to fabricate the BTS/BT 2D

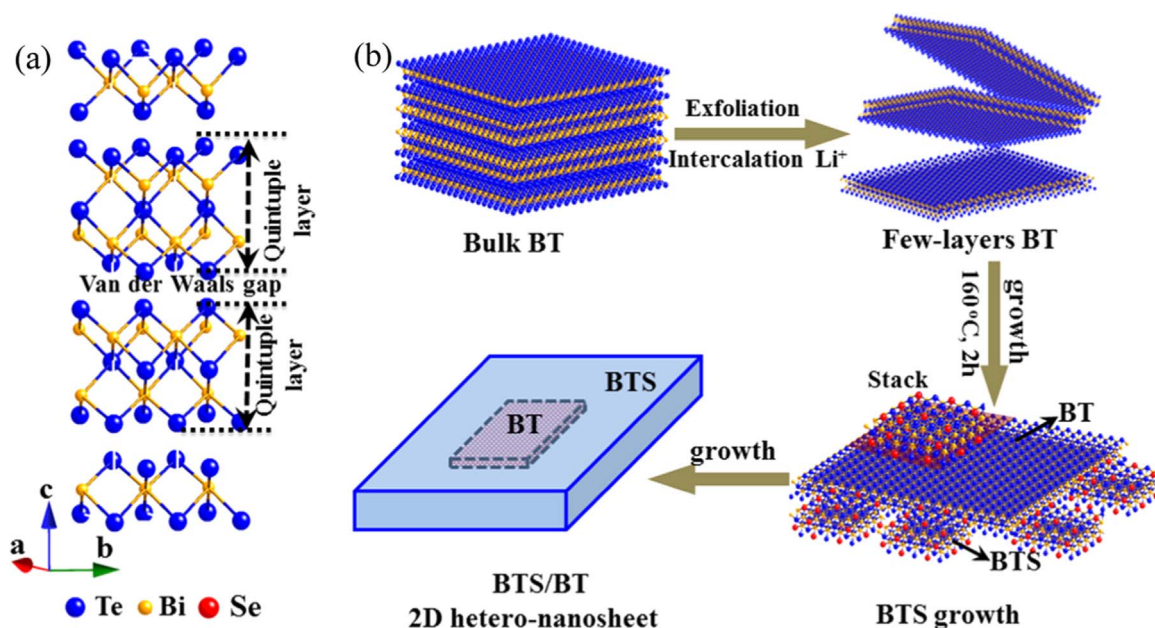


Fig. 1. Crystal structure and synthesis strategy. (a) Schematic crystal structure of  $\text{Bi}_2\text{Te}_3$ . (b) A schematic synthesis process of BTS/BT 2D hetero-nanosheet.

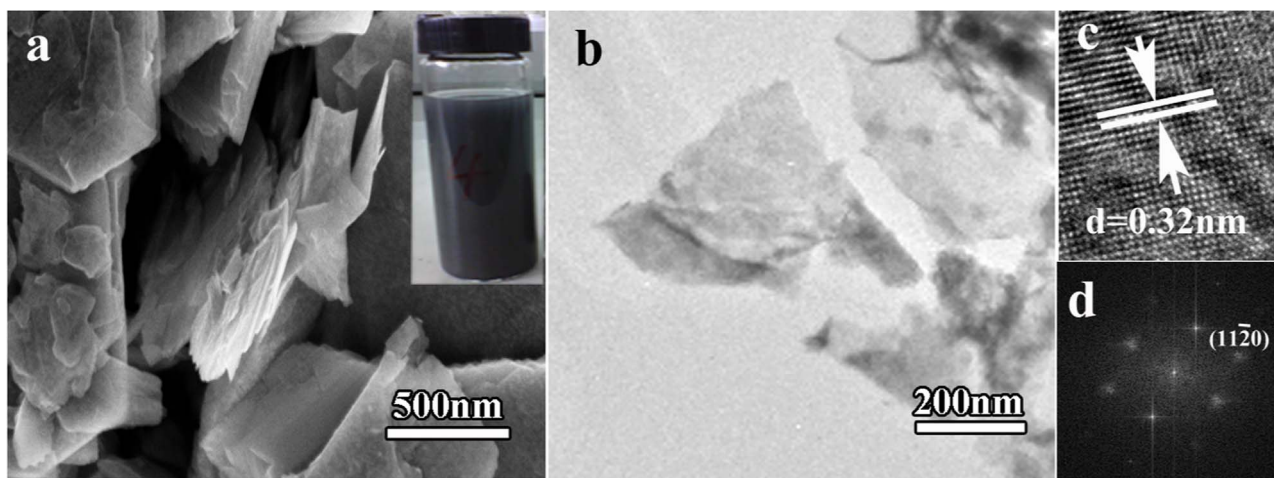


Fig. 2. (a) SEM image of the few-layer  $\text{Bi}_2\text{Te}_3$  and the corresponding colloidal suspension. (b) TEM image, (c) HRTEM image and (d) the corresponding FFT pattern of few-layer  $\text{Bi}_2\text{Te}_3$ .

hetero-nanosheet.

Subsequently, the BTS layers are epitaxially grown along the as-exfoliated BT seeds by a solution-based strategy to form the hetero-nanosheets (Fig. 1). The synthesis of the BTS/BT 2D hetero-nanosheets involves the following steps. First, the stoichiometric amounts of  $\text{TeO}_2$ ,  $\text{SeO}_2$ , and  $\text{NaOH}$  are dissolved to EG solution in a 250 ml three-neck flask to form Te precursors. Then, the Bi precursors solution containing stoichiometric amounts of  $\text{Bi}(\text{NO}_3)_3 \cdot 5\text{H}_2\text{O}$  and Vitamin C are mixed with as-exfoliated  $\text{Bi}_2\text{Te}_3$ . Finally, the reaction is triggered at 165 °C by the rapid injection of the Bi precursor solution to the three-neck flask, and the initially transparent mixture turns into dark purple immediately after the injection. The BTS/BT samples with a mass up to 3.1 g can be obtained in a single batch (Fig. S3), and the overall yield is estimated to be over 90%, which indeed demonstrates the potential for scaling-up of this simple synthetic approach. Owing to its intrinsically anisotropic crystal structure, the hetero epitaxial growth of BTS along BT predominantly takes place on the side surfaces instead of the basal planes (the top and bottom faces), which results in the formation of BTS/BT 2D hetero-nanosheet. Based on the SEM images and corresponding XRD patterns (Fig. S4) obtained at different growth stages of the hetero-nanosheet, it is believed that ripening and ion diffusion

process should be the main driving force for the formation of the unique nanostructure [30–33]. Moreover, because of the ion diffusion of BTS and BT at the ripening stage, amorphous  $\text{Bi}_2\text{Se}_x\text{Te}_{3-x}$  solid solution is generated at the BTS/BT interface, which can construct the so-called low-energy interface as discussed below.

Neutron powder diffraction (NPD) study has been used to investigate the structural details of the BTS/BT sample (Fig. S5). The sample crystallizes in the R-3m space group with unit-cell parameters  $a=4.38$ ,  $b=4.38$ , and  $c=30.46$  Å. It is noted that all the Se atoms doped in Te1 sites, which may relate to the basic crystal structure of BT. The BTS/BT samples with different few-layers BT contents have been characterized by XRD (Fig. S6). The typical XRD pattern of as-synthesized pure BT nanosheets can be indexed exclusively as a rhombohedra BT phase (space group: R-3m, JCPDS data card no.15-0863). The as-prepared BTS nanosheets have been found to exhibit the same phase without detectable impurities, except that the (015) peak slightly shifts toward high angle. Broadening and shifting of the XRD peak for the BTS mean that Se doping introduces disorder to the crystal structure, which agrees well with the previous report [30]. The XRD pattern of BTS/BT shows no obviously difference from the pure BT and BTS, indicating that the introducing of few-layers BT does not destroy the basic

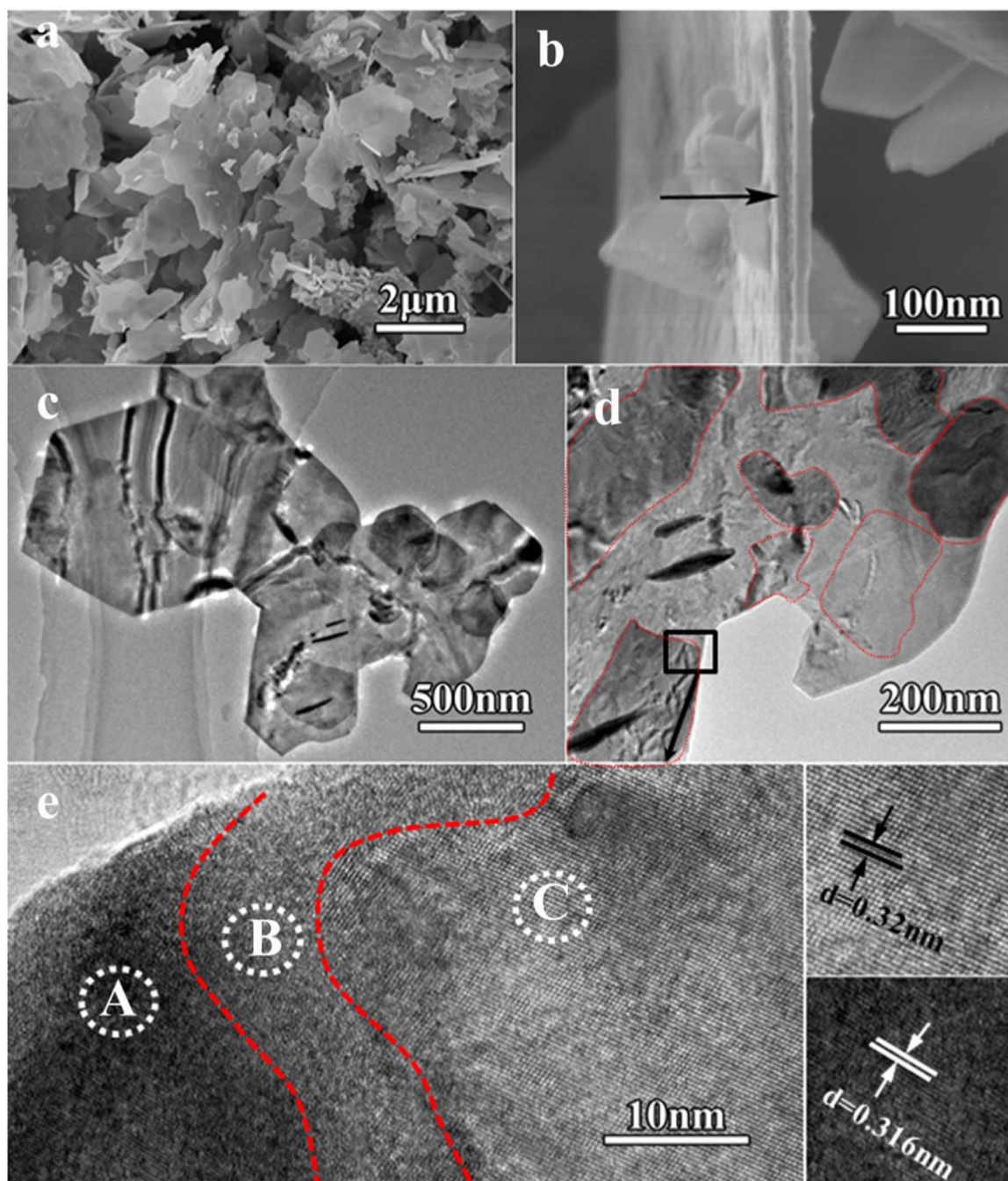


**Fig. 3.** SEM images (a, b) of the sample BTS/BT90. (c) and (d) TEM images, red region indicates 2D hetero-structure. (e) HRTEM image, (e) HRTEM image of region A and (f) region C.

structure of products. As the content of few-layers BT is increased from 30 mg to 150 mg, the broadened and weakened XRD patterns reveal the gradual decrease in crystallinity.

The microstructural details of the as-synthesized BTS/BT90 samples have been characterized by SEM and TEM (Fig. 3). The as-grown samples are mostly irregular nanoplatelets with lateral dimensions of more than 5  $\mu\text{m}$  and a thickness of a few tens of nanometres (Fig. 3a and b). The preferential growth into 2D structures should be attributed to the intrinsically anisotropic bonding nature of BT. For comparison, the pure BT and BTS samples prepared in the same condition without adding the few-layers BT as seeds show quite differences in stacking of small and thin nanoplates (Fig. S3). The lateral dimension of the BT nanosheet is only about 500–1000 nm, much less than epitaxially grown BTS/BT90 2D-sheets. Moreover, there are no discernible stacking of thin nanoplates observed in the BT sample, indicating that

the few-layers BT seeds play an important role in the formation of the unique 2D hetero-nanostructure. The side-view SEM image of the BTS/BT90 (Fig. 3b) shows the thickness is about 30 nm. All the above results prove that the samples have the unique 2D hetero-nanostructures, and the formation mechanism is strongly related to the epitaxial growth from few-layers BT seeds. The TEM image (Fig. 3c) further confirms that the 2D hetero-nanosheets in irregular shape are assembled from the small nanosheet seeds. Interestingly, the non-uniform contrast in the TEM image (in the red frame) indicates that each nanoplate is not a single crystal and the chemical constituent is non-uniform. To investigate the nature of the non-uniform region, HRTEM has been carried out near the interface (the rectangle region marked in Fig. 3d). It is found in the HRTEM image that there are two typical regions with a 5–10 nm amorphous interface, which could be attributed to the BT-seed regions and as-grown BTS regions, respec-

tively. The BT region (marked as region C) with high degree of crystallinity shows a distinct interlayer spacing of approximately 0.32 nm, as expected in the case of (015) planes. However, the as-grown BTS region (marked as region A) reveals a slightly smaller distinct interlayer spacing of 0.316 nm and low degree of crystallinity, which agrees with the XRD result that the (015) peak slightly shifts toward high angle after the Se doping. Remarkably, at the interface of the two regions (marked as region B), a 5–10 nm amorphous  $\text{Bi}_2\text{Se}_x\text{Te}_{3-x}$  solid solution layer is observed (marked as region B), which could be arisen from the ion diffusion on defects of the few-layers BT seed edges under the reaction condition. Moreover, the as-exfoliated few-layers BT have numerous exfoliation-induced defect centers especial in the edge, which may contribute to the formation of amorphous  $\text{Bi}_2\text{Se}_x\text{Te}_{3-x}$  solid solution buffer layer. Thus, the BTS/BT 2D hetero-nanosheets with high density of defects around interfaces have been prepared, which is expected to achieve high thermoelectric performance by scattering phonons with different frequencies.

Spark plasma sintering (SPS) is well known to be a very useful hot-pressing technique for preparing nanostructured bulk materials owing to its very fast heating and cooling rates, which enables fast sintering to prevent unwanted grain growth arising from a long sintering process at high temperatures. In this work, the as-grown 2D-nanosheet samples are sintered using SPS at 573 K for 5 min to obtain bulk pellets. Comparing the XRD patterns of bulk samples with their corresponding powders, there is no change in the diffraction peak due to oxidation or impurity during SPS sintering (Fig. S7), which agrees well with the XPS results (Fig. S8). After SPS sintering, the diffraction peaks become weaker and broader, exhibiting a significant randomness of the tiny size grains, which agrees with the previous report [26,34]. The peak width broadening and intensity weakening reveal a decrease in the content of few-layers BT due to atomic diffusion. Meanwhile, the high density defects around interfaces suppress the grain growth, leading to finally reduced thermal conductivity in the bulk samples composed by these small grains. The grain size of bulk materials varies from 50 to 200 nm which is calculated by the XRD patterns using the Scherrer equation. It is to note that the grain size becomes larger while the content of few-layers BT decreases, which is also confirmed by the FE-SEM images (Fig. S9). The relative density decreases from 92–80% as the few-layers BT content increases, implying that lots of voids also present in these bulk materials. Thus, the high density defects and hetero-interfaces, grain boundaries, and voids could strongly scatter the phonons on all relevant length scales, which would lead to the maximum reduction in lattice thermal conductivity to enhance the thermoelectric performance.

Herein, the transport properties, including the electrical conductivity ( $\sigma$ ), Seebeck coefficient ( $S$ ), and power factor ( $S^2\sigma$ ) of the hybrid TE bulk samples are measured in the temperature range of 300–480 K. As shown in Fig. 4a, all the bulk materials show high electrical conductivity in the order of  $10^2 \text{ S cm}^{-1}$ , comparable to those of other reports on BT-nanostructured bulk materials [34–36]. The decreasing trend of electrical conductivity with the rise of measurement temperature shows a typical metallic behavior, also similar to some previous reports [37]. Compared with pure BT and BTS ( $\sim 700 \text{ S cm}^{-1}$ ), the samples with hetero-structure exhibit a slightly lower electrical conductivity (300–500  $\text{S cm}^{-1}$ ), which is mainly attributed to the enhanced carrier scattering and decreased carrier mobility (Table S1). The high density defects and heterojunction interfaces could enhance carrier scattering and decrease carrier mobility, giving rise to the decrease in electrical conductivity of the BTS/BT. The electrical conductivity decreases with the increasing content of few-layers BT could be attributed to the increase of interfaces and defects. The electrical conductivities decrease slightly with the increase of the measurement temperature, which agrees with the degenerate semiconductor behavior observed in  $\text{Bi}_2\text{Te}_3$  based thermoelectric materials. The negative Seebeck coefficient of all samples reveals a n-type electrical transport property, which is in agreement with the Hall coefficient measurement and previous reports

on  $\text{Bi}_2\text{Te}_{3-x}\text{Se}_x$  [26,28,44]. The absolute value of Seebeck coefficient increases significantly as the content of few-layers BT increases, indicating the well-known behavior of heavily doped semiconductors.

To clarify the electronic transport behavior in our nanocomposites, the Seebeck coefficient as a function of carrier concentration is plotted in Fig. 5. For a single parabolic band and energy-independent carrier scattering approximation for degenerated semiconductors,

$$S = \frac{8\pi^2 k_B^2}{3eh^2} \left( \frac{\pi}{3n} \right)^{\frac{2}{3}} m_d^* T$$

where  $m_d^*$  is the density of states (DOS) effective mass and  $k_B$ ,  $e$ , and  $h$  are the Boltzmann constant, elementary charge, and the Planck constant, respectively. As shown in Fig. 5a, for the pure BT and BTS,  $m_d^*$  is about 0.7  $m_0$ . However,  $m_d^*$  increases to 0.8  $m_0$  (BTS/BT) by introducing the heterojunction interface to the sample, which could be responsible for large  $|S|$  due to the modification of the electronic structure [44]. It should be noted that the BTS/BT samples show relatively large  $m_d^*$  (Fig. 5a) comparing with previously reported n-type BT-based materials [50–52]. As the content of few-layers BT increases, the absolute values of  $S$  increases from 110  $\mu\text{V K}^{-1}$  to 152  $\mu\text{V K}^{-1}$  due to a decrease in the electrical conductivity. The as-prepared bulk samples exhibit low carrier concentration in the range of  $2\text{--}4 \times 10^{19} \text{ cm}^{-3}$ , which is much lower than that of other reports on BT-nanostructured bulk materials [30,34,38], but comparable to that of the  $\text{Bi}_{0.5}\text{Sb}_{1.5}\text{Te}_3$  with dense dislocation arrays embedded in grain boundaries reported by Kim et al. [39].

For BTS/BT hetero-nanosheets, the interface between BTS and few-layers BT might induce an energy dependent carrier scattering effect by introducing a well defined energy barrier which can filter low energy electrons. The pure BT bulk sample has a narrow band gap of about  $\sim 160 \text{ meV}$ . However, after Se-doping, both  $E_c$  and  $E_v$  in BTS shift toward low energy and the band gap is enlarged (175 meV). Moreover, as the bulk BT is exfoliated along the c-axis to the single-layer, the band gap is significantly enlarged (around 240 meV). Thus, the band bending at the heterojunction interface creates a Schottky barrier with a conduction band energy offset  $\Delta E = 70 \text{ meV}$ , which is critical accounting for the increase in Seebeck coefficient through energy filtering effect, such as by passing high-energy (HE) electrons and scattering low-energy (LE) electrons as shown in Fig. 5b. Meanwhile, considering the thickness of the as-exfoliated BT, the change of the electron density of states at the Fermi level as well as the 2D electron gas covering the heterojunction interface further enhance  $S$  due to the quantum confinement effect. As a result of the moderate electrical conductivity and improved Seebeck coefficient, an acceptable power factor about  $1.05 \text{ mW m}^{-1} \text{ K}^{-2}$  of BTS/BT90 is obtained, with no obvious decline compared with the BTS (Fig. 4c). Therefore, through constructing the hybrid BTS/BT hetero-nanosheet, we explore a new approach to regulate the transport properties of thermoelectric materials. We anticipate that further increase in power factor could be achieved by optimizing the potential barrier at the heterojunction interface and the defect engineering.

As expected, the introducing of the Se-doping and heterojunction interface to the nanosheets can significantly reduce the total thermal conductivity ( $\kappa_{\text{tot}}$ ), as shown in Fig. 4d. The minimum value reaches  $0.31 \text{ mW m}^{-1} \text{ K}^{-1}$  for BTS/BT150 at room temperature, which is the same to the predicted minimum thermal conductivity of  $0.31 \text{ W m}^{-1} \text{ K}^{-1}$  in nanograined BT calculated using the Debye-Callaway model [40]. Moreover, the value is much lower than that of the sample BT ( $0.87 \text{ W m}^{-1} \text{ K}^{-1}$ ) and BTS ( $0.69 \text{ W m}^{-1} \text{ K}^{-1}$ ), confirming the heterojunction structure has a great influence on the thermal conductivity. The total thermal conductivity ( $\kappa_{\text{tot}}$ ) decreases gradually as the content of few-layers BT increases, which can be attributed to the increased number of grain boundaries and interfaces as shown by SEM images of the fractured surfaces (Fig. S9). The total thermal conductivity ( $\kappa_{\text{tot}}$ ) of a semiconductor consists of the electronic thermal

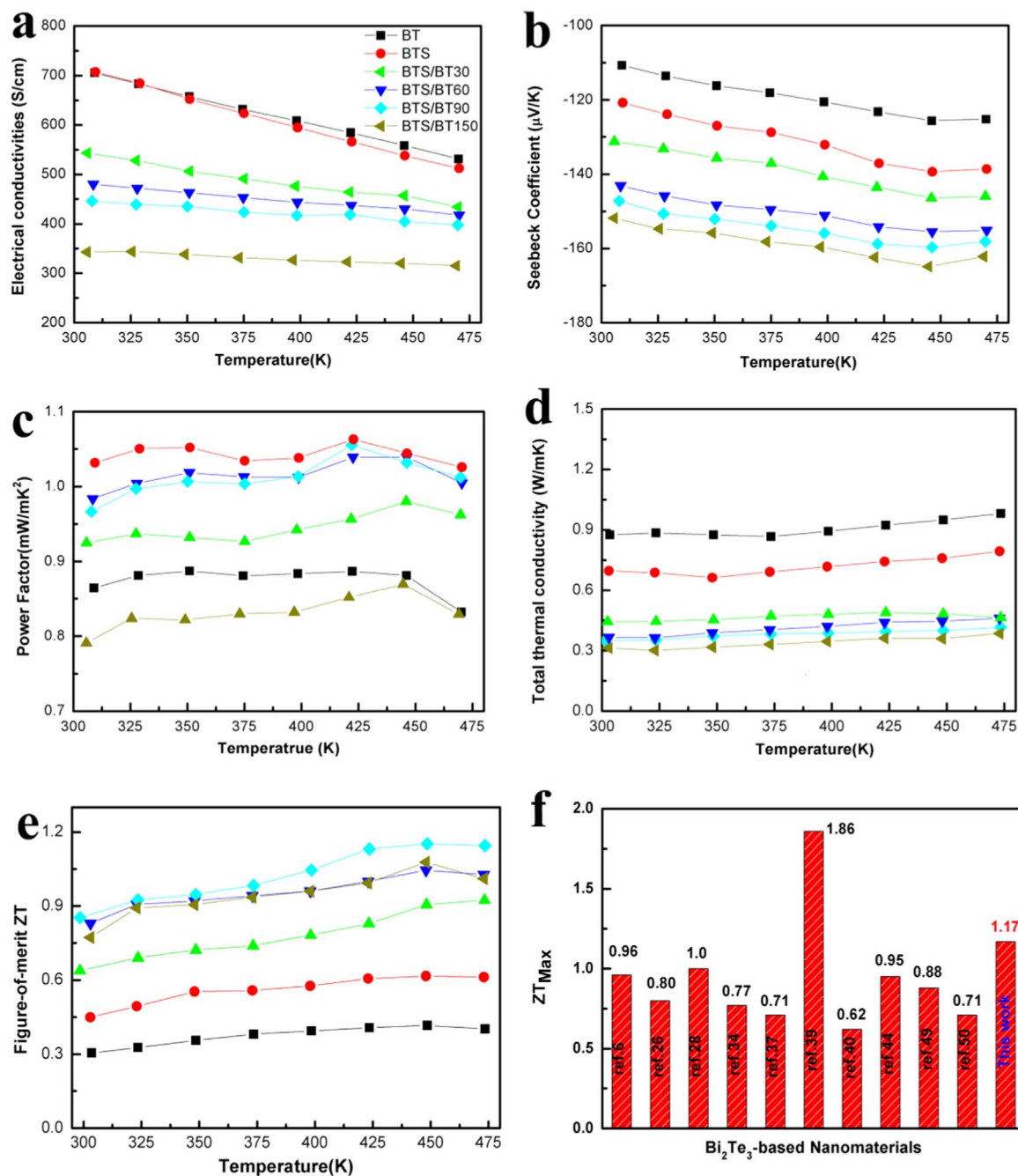


**Fig. 4.** Temperature-dependence of (a) electrical conductivity ( $\sigma$ ), (b) Seebeck coefficient ( $S$ ), and (c) power factors ( $S^2\sigma$ ) of the as-prepared sample. (d) total thermal conductivity ( $\kappa_{tot}$ ), (e) thermoelectric figure of merit  $ZT$ . (f) Comparison of the maximum  $ZT$  of this work with previous reported Bi<sub>2</sub>Te<sub>3</sub>-based nanomaterials. (Ultrathin Bi<sub>2</sub>Te<sub>3</sub> nanowires, exfoliated Bi<sub>2</sub>Te<sub>2.7</sub>Se<sub>0.3</sub> nanosheets, few-layered n-type Bi<sub>2</sub>Te<sub>3</sub>, silver nanoparticles-dispersed Bi<sub>2</sub>Te<sub>3</sub> composites, homogeneous mixing of Bi<sub>2</sub>Te<sub>3</sub> and Bi<sub>2</sub>Se<sub>3</sub> nanosheet, Bi<sub>0.5</sub>Sb<sub>1.5</sub>Te<sub>3</sub> with dense dislocation arrays formed at low-energy grain boundaries, ultrathin Bi<sub>2</sub>Te<sub>3</sub> nanoplates, Au nanodot-included Bi<sub>2</sub>Te<sub>3</sub> nanotube composites, hexagonal plate-like Bi<sub>2</sub>Te<sub>3</sub> nanostructures).

conductivity ( $\kappa_{el}$ ), lattice thermal conductivity ( $\kappa_{latt}$ ), expressed as  $\kappa_{tot} = \kappa_{el} + \kappa_{latt}$  [41]. According to the Wiedemann-Franz law, the  $\kappa_{el}$  is estimated from  $\kappa_{el} = L\sigma T$ , where  $L$  is the Lorentz number calculated using the Fermi integral function (S12). It is found that  $\kappa_{el}$  has small contribution to the  $\kappa_{tot}$  and shows little change in all samples, which indicates that  $\kappa_{latt}$  makes major contribution to the  $\kappa_{tot}$ . However, considering the low relative density of the sample, the porosity should be taken into account to correct the  $\kappa_{latt}$ . As described in the previous work, the modified formulation of the effective medium theory is  $\kappa_{eff} = \kappa_h (2 - \phi) / (2 + \phi)$ , where  $\kappa_{eff}$  is the effective thermal conductivity,  $\kappa_h$  is the thermal conductivity of the porous material, and  $\phi$  is the porosity [40,42–44]. The corrected  $\kappa_{latt}$  for the BT and BTS are  $0.63 \text{ W m}^{-1} \text{ K}^{-1}$

and  $0.45 \text{ W m}^{-1} \text{ K}^{-1}$ , respectively (Fig. S10), which is similar to the nanostructured BT-based materials [45,46]. However, after introducing hybrid BTS/BT heterojunction structure, the  $\kappa_{latt}$  is sharply reduced to about  $0.2\text{--}0.3 \text{ W m}^{-1} \text{ K}^{-1}$ , which is close to the lower limit of the randomly oriented  $\kappa_{latt}$  ( $0.18 \text{ W m}^{-1} \text{ K}^{-1}$ ) [43].

To better understand the relationship between structural characteristics and our remarkably low  $\kappa_{latt}$ , TEM investigation has been employed to analyze the structural characteristics of the SPS pellets. Fig. 6 shows a typical TEM image of BTS/BT90, indicating the multigrain feature. Interesting, the grain boundary with the presence of periodic arrays of dislocations is observed in the sample (Fig. 6c), which has been confirmed to effectively scatter the midfrequency

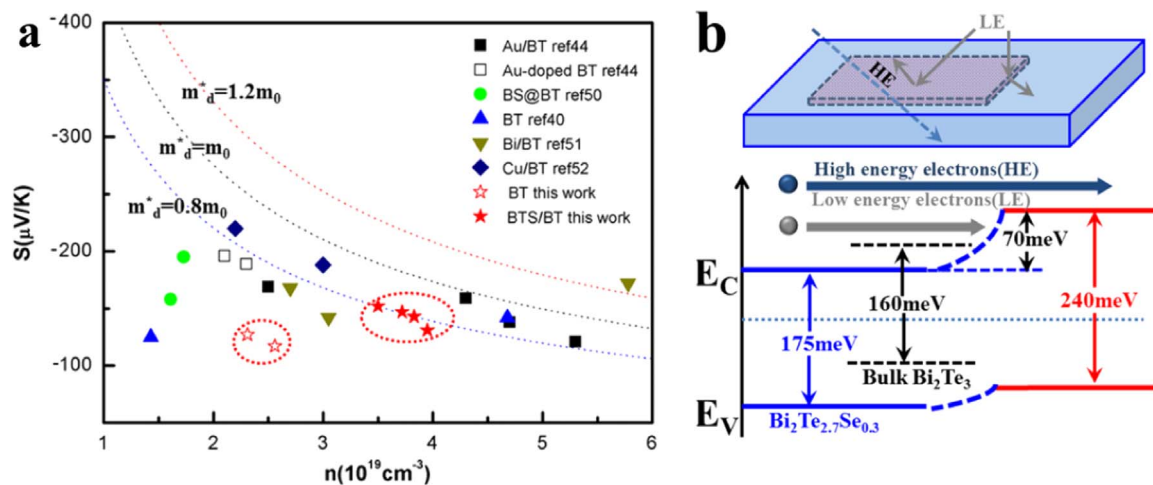


**Fig. 5.** Seebeck coefficient ( $S$ ) as a function of carrier concentration ( $n$ ) for BT, BTS and BTS/BT. The  $S$  values are compared with reported values of Au/BT, Au-doped BT (ref. [50]), BS@BT (ref. [50]), Bi/BT (ref. [51]), Cu/BT (ref. [52]), and BT (ref. [40]). (b) Schematic of the band structure with filtering effect.

phonons [39]. Fig. 6d shows the lattice image of a grain along the [001] direction, the lattice spacing of 1.02 nm corresponds to the lattice spacing between the (003) planes. Two representative regions with distinct interface are observed (marked with red lines in Fig. 6d), which further confirms the existence of 2D BTS/BT heterojunction interface in our samples. The BT regions with a size of about 2–3 nm have a highly distorted lattice along the [001], which could be attributed to the lattice mismatch and exfoliation-induced defect of few-layers BT inclusion. Moreover, various and abundant atomic scale distortions, such as tiny distorted regions and dislocations (marked with red lines in Fig. 6e) are detected. It is readily seen that such a high density of low-energy grain boundaries and heterojunction interfaces coupled with abundant atomic scale distortions can greatly enhance phonon scattering to target the wide spectrum of phonons so as to maximum reduction in  $\kappa_{\text{latt}}$ .

Thus the whole contributors to the  $\kappa_{\text{latt}}$  decrease could be attributed to all scale phonon scattering across multiple length scales [39,47]. The atomic-scale alloy and defect in BTS could scatter high frequency phonons, which contributes about 20% to the  $\kappa_{\text{latt}}$  estimated based on the difference between the BT and BTS. The heterojunction interface with the scale between atomic-scale alloy and nanoscale grains in our samples could introduce a new mechanism, which could effectively scatter the mid-frequency phonons [39]. Compared the room-temperature  $\kappa_{\text{latt}}$  of BTS/BT90 ( $0.21 \text{ W m}^{-1} \text{ K}^{-1}$ ) with the BTS ( $0.45 \text{ W m}^{-1} \text{ K}^{-1}$ ), it is found that the introduced BTS/BT heterojunction interface contribute about 50% reduction to the  $\kappa_{\text{latt}}$ . Therefore, in order to examine the important role of heterojunction interface to the reduction of  $\kappa_{\text{latt}}$ , the sample (noted as BTS/BT90mixture) has been prepared for comparison by mixing the as-prepared BTS nanosheet with few-layers BT using ultrasonic dispersion treatment. The BTS/BT90 mixture shows a much higher electrical conductivity ( $480\text{--}420 \text{ S cm}^{-1}$ ) as well as higher Seebeck coefficient ( $-158\text{--}162 \mu\text{V K}^{-1}$ ) than BTS/BT90. The power factor of the BTS/BT90mixture is about  $1.26 \text{ mW m}^{-1} \text{ K}^{-2}$  (Fig. S11), which is higher than BTS/BT90 and BTS. As mentioned above, the high density defects and heterojunction interfaces of hybrid BTS/BT90 result in an decreased power factor due to enhanced carrier scattering and reduced carrier mobility. However, the  $\kappa_{\text{tot}}$  of BTS/BT90mixture in the range of  $0.65\text{--}0.76 \text{ W m}^{-1} \text{ K}^{-1}$  represents a 70% higher than that of the BTS/BT90, which is mainly attributed to the higher  $\kappa_{\text{latt}}$  of BTS/BT90mixture. These results further confirm that the hybrid 2D hetero-nanostructure is crucial to decrease  $\kappa_{\text{latt}}$  by all-scale phonon scattering. As expected, the maximum ZT value is only 0.74 at 450 K for BTS/BT90mixture, which is much less than that of BTS/BT90 (1.17 at 450 K). Therefore,

the strategy used in our work achieves the maximum reduction in  $\kappa_{\text{latt}}$  by phonon scattering targeting the wide spectrum of phonons and finally improves the ZT of thermoelectric materials.

Taking advantage of the maximum reduced  $\kappa_{\text{tot}}$  as well as a maintained power factor, the figure of merit ZT of the sample is improved significantly, as shown in Fig. 4e. The maximum ZT value is 0.42 at 450 K for BT and 0.62 at 450 K for BTS, similar to the reported data on nanostructured BT-based materials [34,48,49]. However, the herein hybrid BTS/BT with heterojunction interfaces exhibits a remarkable increase in ZT, reaching 1.17 at 450 K and 0.9 around room temperature (300 K) for the BTS/BT90, approximately three times higher than that of BT, which is an excellent and highly competitive value compared to the best results of currently explored BT-nanostructures TE materials (Fig. 4f). Thus, a facile and cost effective strategy has been proposed to prepare BTS/BT hybrid TE materials, which offers opportunities to improve the thermoelectric performance through maximum reducing thermal conductivity (Fig. 6e) and meanwhile maintaining a high power factor. We anticipate that further increase in thermoelectric performance could be realized by optimizing the energy barriers of heterojunction interface and controlling the defect type and density.

#### 4. Conclusions

In summary, by a novel and simple synthetic strategy combining the chemical exfoliation of few-layers BT and solution-based growth of BTS, we have successfully synthesized the hybrid BTS/BT hetero-nanosheet with rational designed heterojunction interfaces to optimize the electron (phonon) transport behavior. The formation of this hybrid hetero-nanostructure is mainly attributed to a cooperative process with few-layers BT as seeds and the heterogeneous nucleation and growth of BTS along its basal planes, which is closely associated with their characteristics of high density of defects and heterojunction interfaces. The designed chemical composition, heterojunction interfaces, and defects in the sample are found to be effective in improving ZT by reducing the  $\kappa_{\text{latt}}$  while maintaining the power factor. The potential barrier about 70 meV at the interface of the few-layers BT and BTS results in an enhanced Seebeck coefficient, a slightly reduced electrical conductivity and finally a power factor of about  $1.05 \text{ mW m}^{-1} \text{ K}^{-2}$  by the low-energy electron filtering effect. A full-spectrum phonon scattering has been achieved by the combination of atomic-scale alloy and defect to target high frequency phonons, heterojunction interface to target the mid-frequency phonons, and nanoscale grains boundary to target low-frequency phonons. Taking advantage of the maximum

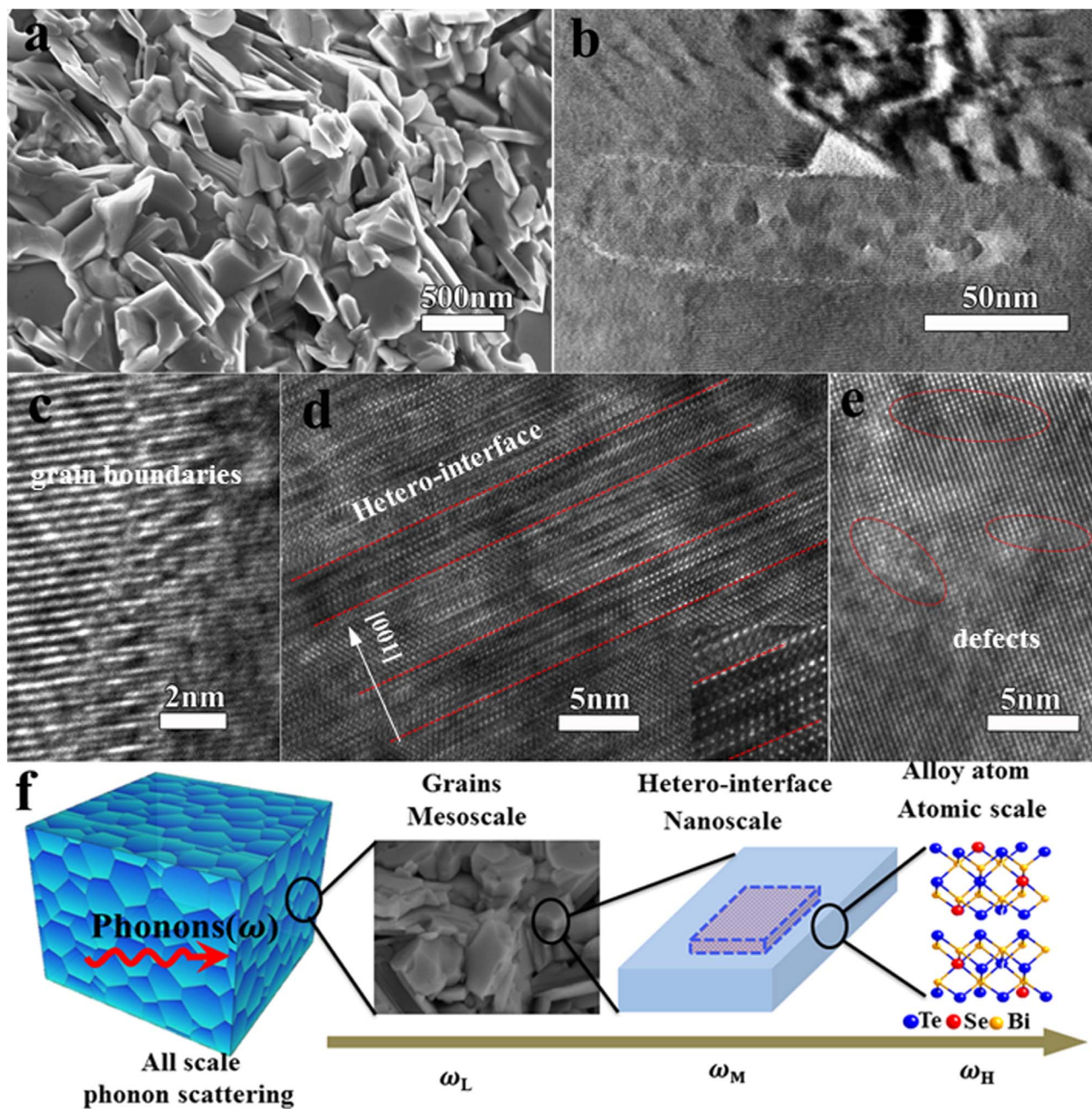


**Fig. 6.** (a) FE-SEM images of the fractured surfaces of BTS/BT 2D hetero-nanosheet after SPS sintering. (b) TEM image of sintered BTS/BT90 showing nanosized grains with clear grain boundaries. (c) (d) (e) HRTEM images of the different regions. (f) Heat-carrying phonons cover a broad spectrum of frequencies ( $\omega$ ). All scale phonon scattering in the as-prepared thermoelectric materials has been achieved, nanoscale grain boundary targets low-frequency phonons ( $\omega_L$ ), heterojunction interface targets the mid-frequency phonons ( $\omega_M$ ), and atomic-scale alloy and defect targets high frequency phonons ( $\omega_H$ ).

reduced  $\kappa_{\text{tot}}$  as well as a maintained power factor, the figure of merit ZT of the sample is greatly improved. A maximum ZT of 1.17 is obtained at 450 K for the BTS/BT90, approximately three times higher than that of the sample without the hybrid hetero-nanostructure. Thus, the strategy proposed in our work provides a new viable avenue to design hybrid structures with ultralow thermal conductivity for high thermoelectric performance.

#### Acknowledgment

The research was financially supported by Guangdong Innovation Team Project (No. 2013N080), Shenzhen Science and Technology Research Grant (Nos. ZDSY20130331145131323,

CXZZ20120829172325895, JCYJ20120614150338154, JCYJ20150827155136104).

#### Appendix A. Supporting information

Supplementary data associated with this article can be found in the online version at [doi:10.1016/j.nanoen.2016.09.018](https://doi.org/10.1016/j.nanoen.2016.09.018).

#### References

- [1] M.G. Kanatzidis, *MRS Bull.* 40 (2015) 687–694.
- [2] N.A. Heinz, T. Ikeda, Y. Pei, G.J. Snyder, *Adv. Funct. Mater.* 24 (2014) 2135–2153.
- [3] L.E. Bell, *Science* 321 (2008) 1457–1461.
- [4] J.R. Sootsman, D.Y. Chung, M.G. Kanatzidis, *Angew. Chem. Int. Ed.* 48 (2009)

- 8616–8639.
- [5] M.S. Dresselhaus, G. Chen, M.Y. Tang, R. Yang, H. Lee, D. Wang, Z. Ren, J.-P. Fleurial, P. Gogna, *Adv. Mater.* 19 (2007) 1043–1053.
- [6] G. Zhang, B. Kirk, L.A. Jauregui, H. Yang, X. Xu, Y.P. Chen, Yue Wu, *Nano Lett.* 12 (2012) 56–60.
- [7] G. Tan, F. Shi, S. Hao, H. Chi, T.P. Bailey, L.-D. Zhao, C. Uher, C. Wolverton, V.P. Dravid, M.G. Kanatzidis, *J. Am. Chem. Soc.* 137 (35) (2015) 11507–11516.
- [8] A.-L. Hansen, T. Dankwort, M. Winkler, J. Ditto, D.C. Johnson, J.D. Koenig, K. Bartholome, L. Kienle, W. Bensch, *Chem. Mater.* 26 (22) (2014) 6518–6522.
- [9] H. Ohta, S.W. Kim, Y. Mune, T. Mizoguchi, K. Nomura, S. Ohta, T. Nomura, Y. Nakanishi, Y. Ikuhara, M. Hirano, H. Hosono, K. Koumoto, *Nat. Mater.* 6 (2007) 129–134.
- [10] M. Zebarjadi, G. Joshi, G. Zhu, B. Yu, A. Minnich, Y. Lan, X. Wang, M. Dresselhaus, Z. Ren, G. Chen, *Nano Lett.* 11 (2011) 2225–2230.
- [11] M. Ibáñez, R. Zamani, A. LaLonde, D. Cadavid, W. Li, A. Shavel, J. Arbiol, J.R. Morante, S. Gorsse, G.J. Snyder, A. Cabot, *J. Am. Chem. Soc.* 134 (2012) 4060–44063.
- [12] M. Ibáñez, R. Zamani, S. Gorsse, J. Fan, S. Ortega, D. Cadavid, J.R. Morante, J. Arbiol, A. Cabot, *ACS Nano* 7 (2013) 2573–22586.
- [13] S.W. Finet, G. Zhang, J.-H. Bahk, H. Fang, H. Yang, A. Shakouri, Y. Wu, *Nano Lett.* 14 (2014) 3466–3473.
- [14] M. Ibáñez, D. Cadavid, R. Zamani, N.G. Castello, V.I. Roca, W. Li, A. Fairbrother, J.D. Prades, A. Shavel, J. Arbiol, A.P. Rodriguez, J.R. Morante, A. Cabot, *Chem. Mater.* 24 (2012) 562–5570.
- [15] W. Liu, C.F. Guo, M. Yao, Y. Lan, H. Zhang, Q. Zhang, S. Chen, C.P. Opeil, Z. Ren, *Nano Energy* 4 (2014) 113–122.
- [16] Z.-H. Ge, B.-P. Zhang, P.-P. Shang, J.-F. Li, *J. Mater. Chem.* 21 (2011) 9194–9200.
- [17] R.J. Mehta, Y. Zhang, H. Zhu, D.S. Parker, M. Belley, D.J. Singh, R. Ramprasad, T.B. Tasciuc, G. Ramanath, *Nano Lett.* 12 (2012) 4523–4529.
- [18] W. Xie, J. He, H.J. Kang, X. Tang, S. Zhu, M. Laver, S. Wang, J.R.D. Copley, C.M. Brown, Q. Zhang, T.M. Tritt, *Nano Lett.* 10 (2010) 3283–3289.
- [19] X.A. Fan, J.Y. Yang, Z. Xie, K. Li, W. Zhu, X.K. Duan, C.J. Xiao, Q.Q. Zhang, *J. Phys. D: Appl. Phys.* 40 (2007) 5975–5979.
- [20] L. Hu, T. Zhu, X. Liu, X. Zhao, *Adv. Funct. Mater.* 24 (2014) 5211–5218.
- [21] Y. Zhao, J.S. Dyck, B.M. Hernandez, C. Burda, *J. Phys. Chem. C* 114 (2010) 11607–11613.
- [22] Y. Zhang, G.D. Stucky, *Chem. Mater.* 26 (2014) 837–848.
- [23] B. Liao, G. Chen, *MRS Bull.* 40 (09) (2015) 746–752.
- [24] A.J. Minnich, M.S. Dresselhaus, Z.F. Ren, G. Chen, *Energy Environ. Sci.* 2 (2009) 466–479.
- [25] G. Xiao, C. Zhu, Y. Ma, B. Liu, G. Zou, B. Zou, *Angew. Chem.* 126 (2014) 748–752.
- [26] J. Ko, J.-Y. Kim, S.-M. Choi, Y.S. Lim, W.-S. Seo, K.H. Lee, *J. Mater. Chem. A* 1 (2013) 12791–12796.
- [27] M. Hong, Z.-G. Chen, L. Yang, G. Han, J. Zou, *Adv. Electron. Mater.* 1 (2015). <http://dx.doi.org/10.1002/aeml.201500025>.
- [28] P. Puneet, R. Podila, M. Karakaya, S. Zhu, J. He, T.M. Tritt, M.S. Dresselhaus, A.M. Rao, *Sci. Rep.* 3 (2013) 3212–3219.
- [29] Y. Sun, H. Cheng, S. Gao, Q. Liu, Z. Sun, C. Xiao, C. Wu, S. Wei, Y. Xie, *J. Am. Chem. Soc.* 134 (2012) 20294–20297.
- [30] A. Soni, Y. Zhao, L. Yu, M.K.K. Aik, M.S. Dresselhaus, Q. Xiong, *Nano Lett.* 12 (2012) 1203–1209.
- [31] A. Zhuang, J.-J. Li, Y.-C. Wang, X. Wen, Y. Lin, B. Xiang, X. Wang, J. Zeng, *Angew. Chem.* 126 (2014) 6543–6547.
- [32] J.-Li. Mi, N. Lock, T. Sun, M. Christensen, M. Søndergaard, P. Hald, H.H. Hng, J. Ma, B.B. Iversen, *ACS Nano* 4 (5) (2010) 2523–2530.
- [33] Y. Zhang, H. Wang, S. KrCaemer, Y. Shi, F. Zhang, M. Snedaker, K. Ding, M. Moskovits, G.J. Snyder, G.D. Stucky, *ACS Nano* 5 (4) (2011) 3158–3165.
- [34] Q. Zhang, X. Ai, L. Wang, Y. Chang, W. Luo, W. Jiang, L. Chen, *Adv. Funct. Mater.* 25 (6) (2015) 966–976.
- [35] S. Song, J. Fu, X. Li, W. Gao, H. Zhang, *Chem. Eur. J.* 19 (2013) 2889–2894.
- [36] Y. Zhang, L.P. Hu, T.J. Zhu, J. Xie, X.B. Zhao, *Cryst. Growth Des.* 13 (2013) 645–651.
- [37] Y. Min, J.W. Roh, H. Yang, M. Park, S. Il Kim, S. Hwang, S.M. Lee, K.H. Lee, U. Jeong, *Adv. Mater.* 25 (2013) 1425–1429.
- [38] R.J. Mehta, Y. Zhang, C. Karthik, B. Singh, R.W. Siegel, T.B. Tasciuc, G. Ramanath, *Nat. Mater.* 11 (2012) 233–240.
- [39] S. Il Kim, K.H. Lee, H.A. Mun, H.S. Kim, S.W. Hwang, J.W. Roh, D.J. Yang, W.H. Shin, X.S. Li, Y.H. Lee, G.J. Snyder, S.W. Kim, *Science* 348 (2015) 109–114.
- [40] J.S. Son, M.K. Choi, M.-K. Han, K. Park, J.-Y. Kim, S.J. Lim, M. Oh, Y. Kuk, C. Park, S.-J. Kim, T. Hyeon, *Nano Lett.* 12 (2012) 640–647.
- [41] H. Yang, J.-H. Bahk, T. Day, A.M.S. Mohammed, G.J. Snyder, A. Shakouri, Y. Wu, *Nano Lett.* 15 (2) (2015) 1349–1355.
- [42] H. Lee, D. Vashaee, D.Z. Wang, M.S. Dresselhaus, Z.F. Ren, G. Chen, *J. Appl. Phys.* 107 (2010) 094308–094315.
- [43] M. Takashiri, S. Tanaka, H. Hagino, K. Miyazaki, *J. Appl. Phys.* 112 (2012) 084315–084323.
- [44] E. Lee, J. Ko, J.-Y. Kim, W.-S. Seo, S.-M. Choi, K.H. Lee, W. Shime, W. Lee, *J. Mater. Chem. C* 4 (2016) 1313–1319.
- [45] K.T. Kim, S.Y. Choi, E.H. Shin, K.S. Moon, H.Y. Koo, G.-G. Lee, G.H. Ha, *Carbon* 52 (2013) 541–549.
- [46] L. Hu, T. Zhu, X. Liu, X. Zhao, *Adv. Funct. Mater.* 24 (2014) 5211–5218.
- [47] K. Biswas, J. He, I.D. Blum, C.-I. Wu, T.P. Hogan, D.N. Seidman, V.P. Dravid, M.G. Kanatzidis, *Nature* 489 (2012) 414–418.
- [48] G. Han, Z.-G. Chen, L. Yang, M. Hong, J. Drennan, J. Zou, *ACS Appl. Mater. Interfaces* 7 (1) (2015) 989–995.0.
- [49] L. Yang, Z.-G. Chen, M. Hong, G. Han, J. Zou, *ACS Appl. Mater. Interfaces* 7 (42) (2015) 23694–23699.
- [50] Y. Min, G. Park, B. Kim, A. Giri, J. Zeng, J.W. Roh, S. Il Kim, K.H. Lee, U. Jeong, *ACS Nano* 9 (7) (2015) 6843–6853.
- [51] S. Sumithra, N.J. Takas, D.K. Misra, W.M. Nolting, P.F.P. Poudeu, K.L. Stokes, *Adv. Energy Mater.* 1 (6) (2011) 1141–1147.
- [52] M.-K. Han, K. Ahn, H.J. Kim, J.-S. Rhyee, S.-J. Kim, *J. Mater. Chem.* 21 (2011) 11365–11370.



Dr. Shuankui Li received his PhD degree in Condensed Matter Physics in 2014 from Lanzhou University, China. He is currently a post-doctoral fellow at School of Advanced Materials, Peking University, Shenzhen Graduate School with a research focus on design and preparation high performance nanostructured thermoelectrics materials.



Chao Xin received his B. Sc in 2009 from Yanbian University, China. Then he received his pH. D degree in 2015 from Harbin Institute of Technology. He is currently a post-doctoral fellow at School of Advanced Materials, Peking University, Shenzhen Graduate School, China. His research interests include: computational materials, energy materials (battery materials, solar energy, multiferroic materials, thermoelectric materials), nanomaterials, nanoelectronics.



Xuerui Liu received his B.S. degree in Materials Chemistry from Peking University, China in 2015. He is pursuing his M.S. degree in the School of Advanced Materials, Peking University, China. His research interest is thermoelectric materials



Dr. Yancong Feng received his B.Sc. in 2009 and pH.D degree in 2014 from Beijing University of Chemical Technology, China. He is currently a post-doctoral fellow at School of Advanced Materials, Peking University, Shenzhen Graduate School, China. His research interests include: battery materials, metallic glasses, polymer nanocomposites, solid polymer electrolytes.



Dr Yidong Liu is currently distinguished researcher in School of Advanced Materials, Peking University Shenzhen Graduate School. He received his PhD in Chemistry from the Graduate Center/ CUNY in 2006. After his PhD, he moved to Columbia University as an associate research scientist. His research concentrates in high performance materials, composite and devices.



Dr Yiming Qiu received his PhD in condensed matter physics from Johns Hopkins University in 2002. He currently works as an instrument scientist at the National Institute of Standards and Technology Center for Neutron Research. His research interests center on studying the strongly correlated materials, especially the geometrically frustrated and low dimensional systems, using neutron scattering technique.



Jiaxin Zheng received his BSc in Physics in 2008 and PhD degree in Condensed Matter Physics in 2013 from Peking University, China. Then he joined the group of Prof. Feng Pan at School of Advanced Materials (SAM), Peking University, Shenzhen Graduate School, China, as a post-doctoral fellow from Oct. 2013 to Oct. 2015. Now he works an assistant Professor at SAM. His research interests include: computational materials, energy materials (battery materials, solar energy, thermoelectric materials), nano-materials, nanoelectronics.



Professor Jun Luo received his p.H.D in Condensed Matter Physics from the Institute of Physics, Chinese Academy of Science, in 2005. Then, he was awarded an Alexander von Humboldt Research Fellowship to visit Free University of Berlin. He went back to Institute of Physics, Chinese Academy of Science, in 2007, and worked there for 7 years. In October of 2013, he moved to Shanghai University and continued his work on thermoelectric materials.



Fu-Sheng Liu received his p.H.D. in condensed matter physics in 2005 from Institute of Physics, Chinese Academy of Sciences (CAS), China. From 2005 to now, he joined in Shenzhen University as a full professor. His current research interests include crystal structure, metallic functional materials, thermoelectric materials and their related properties. He has authored and co-authored more than 100 refereed journal publications.



Prof. Feng Pan, National 1000-plan Professor, Founding Dean of School of Advanced Materials, Peking University Shenzhen Graduate School, Director of National Center of Electric Vehicle Power Battery and Materials for International Research, got B.S. from Dept. Chemistry, Peking University in 1985 and PhD from Dept. of P & A Chemistry, University of Strathclyde, Glasgow, UK, with “Patrick D. Ritchie Prize” for the best p.H.D. in 1994. With more than a decade experience in large international incorporations, Prof. Pan has been engaged in fundamental research and product development of novel optoelectronic and energy storage materials and devices. As Chief Scientist, Prof. Pan led 8 entities in Shenzhen to win the 150 million RMB grant for the national new energy vehicles (power battery) innovation project from 2013 to end of 2015. As Chief Scientist, Prof. Pan led 12 entities to win National Key project of Material Genomic Engineering for Solid State Li-ion Battery in China in 2016.



Qingzhen Huang graduated from University of Science and Technology of China in 1977. In years between 1977 and 1990, he worked in Fujiang Institute of Research on Structure of Matter, Chinese Academy of Science. As an instrument scientist, he has worked at NIST Center for Neutron Research since 1990. His research interests are on studies of relationships between crystal structure and properties using neutron powder diffraction.